Journal of Alloys and Compounds 509 (2011) 3211–3218

Contents lists available at ScienceDirect

Journal of Alloys and Compounds

journal homepage: www.elsevier.com/locate/jallcom

Microstructure characterization of rapidly solidified Al–Fe–Cr–Ce alloy by positron annihilation spectroscopy

Alena Michalcová[a,*], Dalibor Vojtěch[b], Jakub Čížek[c], Ivan Procházka[c], Jan Drahokoupil[d], Pavel Novák[b]

[a] Institute of Chemical Technology, Prague, Department of Chemical Technology of Monuments Conservation, Technicka 5, 166 28 Prague, Czech Republic
[b] Institute of Chemical Technology, Prague, Department of Metals and Corrosion Engineering, Technicka 5, 166 28 Prague, Czech Republic
[c] Department of Low-Temperature Physics, Faculty of Mathematics and Physics, Charles University, V Holešovičkách 2, CZ-180 00 Prague 8, Czech Republic
[d] Institute of Physics – Academy of Sciences CR, Na Slovance 2, 182 21 Prague 8, Czech Republic

ARTICLE INFO

Article history:
Received 25 October 2010
Accepted 7 December 2010
Available online 15 December 2010

Keywords:
Metals and alloys
Nanostructured materials
Rapid solidification
Positron spectroscopies
Transmission electron microscopy
X-ray diffraction

ABSTRACT

Positron annihilation spectroscopy was employed for the microstructure characterization of rapidly solidified Al–3 wt.% Cr–3 wt.% Fe–0.8 wt.% Ce alloy prepared by melt spinning. Results of the positron annihilation study are analyzed within the diffusion trapping model and compared with results of X-ray diffraction, transmission electron microscopy and microhardness measurements. A good consistency among all experimental techniques was obtained. The rapidly solidified alloy exhibits ultra fine grained structure, consisting of cells separated by dislocation walls. Annealed samples showed no significant changes in structure up to 400 °C which proves good thermal stability of ultra fine grained structure. Exposure of the sample to temperature of 500 °C caused significant changes in the material.

1. Introduction

The rapid solidification processing involves exceptionally high cooling rates (10^4–10^8 K/s) during solidification from the molten state. The levels of undercooling achievable at such high cooling rates lead to significant and often potentially beneficial modifications of rapidly solidified microstructures compared to those produced under conventional conditions [1]. The rapid solidification causes an increase in the solubility of alloying elements in the matrix, a refinement of the microstructure and an improvement of material homogeneity. Rapidly solidified materials also contain many structural defects, e.g. dislocations, vacancies and vacancy clusters. In alloys prepared under conventional conditions, these defects are often surrounded by atmospheres of alloying elements, which relax internal stresses caused by the presence of defects. The cooling rates in the rapid solidification process are sufficiently high to suppress diffusion of alloying elements. Thus, it is expected that a rapidly solidified alloy will not contain the atmospheres of alloying elements surrounding the structural defects. Moreover, diffusion of alloying elements is the rate limiting factor for the formation of large intermetallic phases. Hence, because of suppressed diffusion, the concentration of alloying elements dissolved in the matrix in rapidly solidified alloys is often higher than the room temperature solubility limit.

Since rapidly solidified alloys exhibit a highly non-equilibrium structure, exposure of these alloys to elevated temperatures may cause significant changes in the material, caused by increasing diffusivity of elements. These changes can be examined on the macroscopic scale by changes of hardness and on the micro and the nano-scale by transmission electron microscopy (TEM). The grain coarsening and recovery of dislocations can also be detected by line profile analysis of X-ray diffraction (XRD) reflections.

Positron annihilation spectroscopy (PAS) is a well-recognized, non-destructive method with very high sensitivity to open-volume defects like vacancies, vacancy clusters, dislocations etc. [2–4]. PAS involves several experimental techniques: (i) positron lifetime (LT) spectroscopy [2,4] which enables the identification of the type of defects and determines defect concentrations; (ii) coincidence measurements of Doppler broadening (CDB) [5] being a unique method which carries information about the local chemical environment of defects. Due to its non-destructivity and simple sample preparation, PAS can be considered as a promising alternative to the traditional methods of microstructure characterization [4,6,7].

Positrons implanted into a solid quickly lose their energy and thermalize typically during a few ps [8,9]. Thermalized positron is delocalized in the lattice and may be trapped in open-volume defects which represent potential wells for positrons. Positron

* Corresponding author. Tel.: +420 220443683.
E-mail address: michalca@vscht.cz (A. Michalcová).

0925-8388/$ – see front matter © 2010 Elsevier B.V. All rights reserved.
doi:10.1016/j.jallcom.2010.12.049

annihilation rate is given by an overlap of positron and electron density [9]. Hence, the lifetime of a trapped positron carries information about the local electron density in the defect. Therefore, lifetimes of trapped positrons enable the identification of defects in the studied sample. The kinetics of positron trapping in defects can be described by an appropriate trapping model, which allows for the determination of defect densities [2,4].

The CDB technique is based on the fact that the high momentum part of the Doppler broadened profile, which comes from positrons annihilated by core electrons, reflects the electronic structure of a particular element. In other words, it is a kind of 'fingerprint' – a unique characteristic of the particular element [10,11]. The chemical environment of positron traps can be determined from comparison of the high momentum parts of CDB profiles measured on studied samples with those obtained on standards, i.e. well defined specimens prepared from pure elements, or with those calculated theoretically [12,13]. Because of the above mentioned reasons, a combination of LT spectroscopy with CDB offers a unique way of microstructure characterization of rapidly solidified alloys.

2. Experimental

An alloy containing 93.08 wt.% Al–3.17 wt.% Cr–2.92 wt.% Fe–0.83 wt.% Ce, denoted as $AlCr_3Fe_3Ce_1$, was prepared by melt spinning with circumferential speed of cooling wheel of 20 m/s. The as-prepared samples have the shape of a long ribbon with a width of ≈5 mm and a thickness of ≈0.1 mm. The chemical composition of the alloy and the cooling rate were chosen according to the future industrial processing. The chemical composition was determined by X-ray fluorescence spectroscopy (XRF) using spectrometer ARL 9400 XP. The ribbons were examined in cross section by NEOPHOT 2 light microscope (LM). The Vickers hardness HV 0.02 was also determined on the cross sectioned ribbons. Materials prepared using the melt spinning method usually exhibit a structural gradient caused by varying cooling rate with the distance from the cooling wheel. Because of this it is possible to distinguish the 'wheel side', i.e. the side attached directly on the cooling wheel, and the 'free side', i.e. the opposite side of the ribbon.

Long-term annealing of the alloy was performed in an electric resistance furnace. Samples were annealed at 300 °C, 400 °C and at 500 °C to determine the thermal stability of microstructure. After the long term annealing (2.5, 5, 10, 25, 50, 75 and 100 h), HV 0.02 was measured at room temperature.

Samples for TEM were prepared by grinding the 3 mm disc to a thickness of 50 μm. The grinding was always performed on the 'free side' of ribbons. Consequently, the samples were dimpled again on the 'free side' by GATAN Dimple Grinder, Model 656 to the final thickness of 10 μm. This preparation process enables the observation of the 'wheel side' of the ribbon which was quenched by the highest cooling rate. Final precision ion polishing was done by GATAN PIPS, Model 691. TEM samples were examined using a transmission electron microscope JEOL 3010 (LaB_6, accelerating voltage 300 kV). XRD studies were performed on the 'wheel side' of ribbons by PAN ANALYTICAL X'Pert PRO + High Score Plus with Cu anode. The Topas3 program was employed for the Rietveld structure refinement.

The rapidly solidified alloy and samples annealed at 300 °C, 400 °C and 500 °C for 100 h were examined by PAS. During PAS measurements, a $^{22}Na_2CO_3$ positron source with the activity of 1 MBq deposited on a 2 μm thick mylar foil was sandwiched between several ribbons stacked tightly so that there was no air gap in between. The source contribution in LT spectra consisted of two components with lifetimes ≈368 ps and ≈1.5 ns which come from positrons annihilating in the $^{22}Na_2CO_3$ spot and in the covering foil. The intensities of the source components were ≈8% and ≈1%.

A high resolution digital spectrometer [14,15] was employed for LT investigations of the studied alloys. The detector part of the digital LT spectrometer is equipped with two Hamamatsu H3378 photomultipliers coupled with BaF_2 scintillators. Detector pulses are sampled in real time by two ultra-fast 8-bit digitizers Acqiris DC211 with a sampling frequency of 4 GHz. The digitized pulses are acquired in a PC and worked out off-line by software using a new algorithm for integral constant fraction timing [16]. The time resolution of the digital LT spectrometer was 150 ps (FWHM = full width at half maximum, ^{22}Na). At least 10^7 annihilation events were accumulated in each LT spectrum. Decomposition of LT spectra into exponential components was performed using a maximum likelihood based fitting procedure [17].

The CDB spectrometer consists of two high-purity Ge detectors and commercial nuclear instrument modules operated by a PC. The overall energy resolution of the spectrometer was 1.0 keV (FWHM) at 511 keV energy. At least 10^8 events were collected in each two-dimensional spectrum, which was subsequently reduced into one-dimensional Doppler profile and instrumental resolution cuts. The relative changes of Doppler profiles were followed as ratio curves of the normalized Doppler profiles related to the profile of a well annealed pure Fe (99.999%) and Al (99.9999%) reference sample. The CDB profiles are symmetrical with respect to the origin and only the parts corresponding to positive Doppler shifts are shown in the paper.

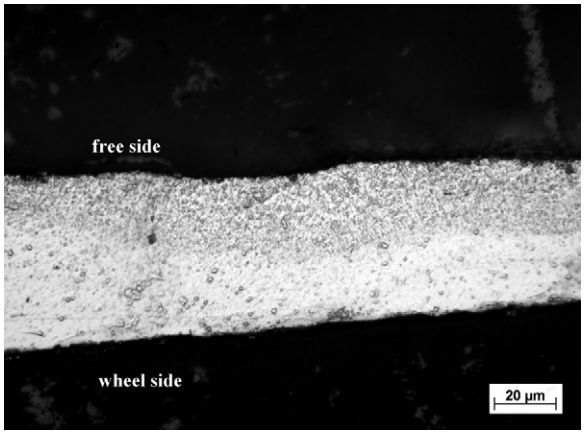

Fig. 1. LM image of cross section of rapidly solidified $AlCr_3Fe_3Ce_1$ alloy ribbon. The 'wheel side' is on the bottom in the figure.

3. Results

Fig. 1 shows LM image of the cross-section of rapidly solidified $AlCr_3Fe_3Ce_1$ alloy. Clearly, the 'wheel side' of the ribbon, which is placed in the bottom in Fig. 1, exhibits finer structure compared to the 'free side'. This is caused by higher cooling rate achieved on the 'wheel side' which is in direct contact with the cooling wheel. TEM micrograph of the rapidly solidified alloy in Fig. 2 documents that the alloy is formed by fcc-Al grains surrounded by intermetallic phases. The XRD pattern measured on rapidly solidified alloy is shown in Fig. 3. The intermetallic phases $Al_{13}Cr_2$ and $Al_{20}CeCr_2$ and a small amount of $Al_{80}(Cr,Fe)_{20}$ quasicrystalline phase were identified. It was shown that Al–Fe interaction in melt is very strong and leads to the formation of Al–Fe quasicrystals [18,19]. Presence of the quasicrystalline phase has beneficial influence because it suppresses grain growth at elevated temperatures [20]. Indeed, the structure of $AlCr_3Fe_3Ce_1$ alloy does not change even after annealing at 400 °C for 100 h, as documented in Fig. 4. Moreover, hardness shown in Fig. 5 also remains constant after annealing at 400 °C. The

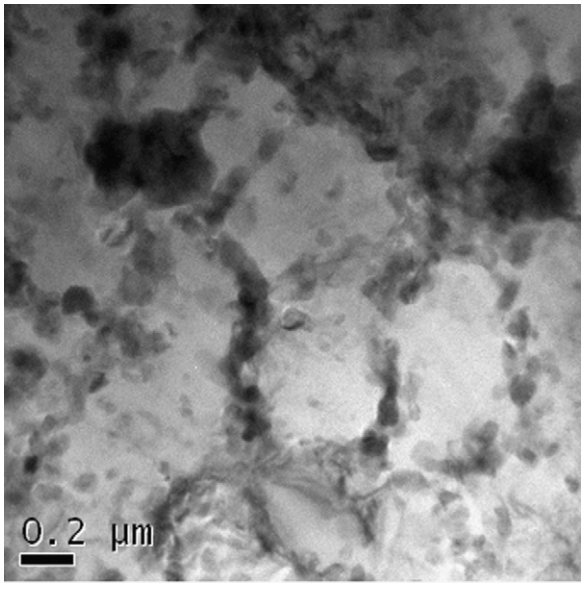

Fig. 2. A representative TEM micrographs of rapidly solidified $AlCr_3Fe_3Ce_1$ alloy.

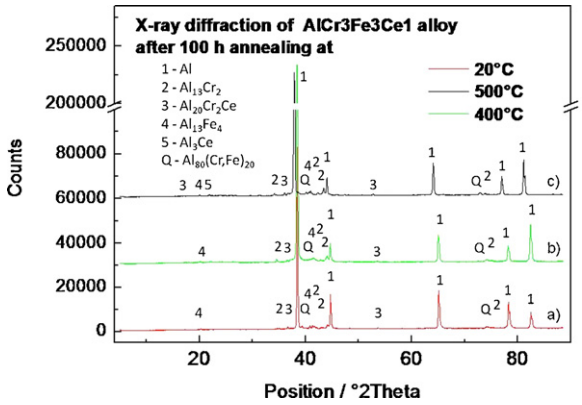

Fig. 3. XRD patterns measured on $AlCr_3Fe_3Ce_1$ alloy: (a) rapidly solidified alloy, sample annealed for 100 h at (b) 400 °C and (c) 500 °C.

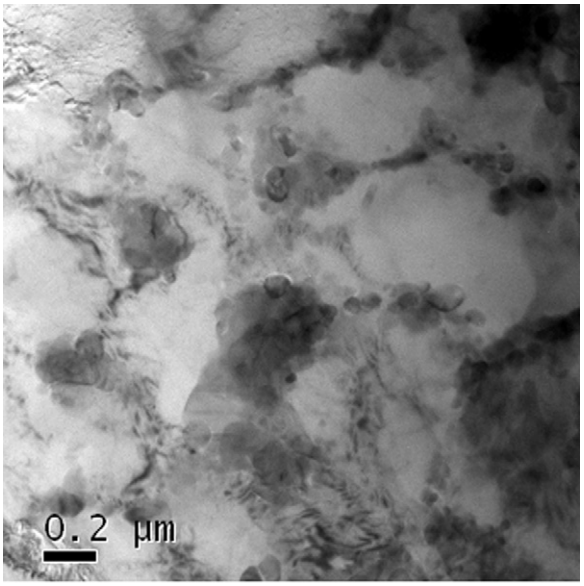

Fig. 4. TEM micrographs of $AlCr_3Fe_3Ce_1$ alloy annealed at 400 °C for 100 h.

XRD pattern in Fig. 3b testifies that the phase composition in the material annealed at 400 °C remains virtually the same as in the rapidly solidified alloy. High thermal stability of the rapidly solidified alloy is obviously due to a low diffusivity of alloying elements in Al matrix.

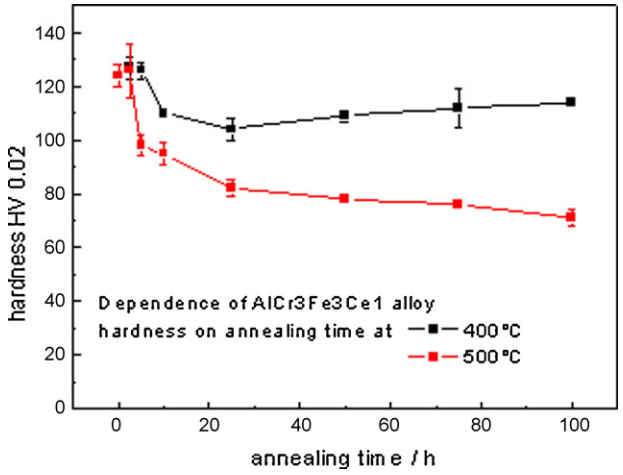

Fig. 5. Dependence of hardness on annealing time for $AlCr_3Fe_3Ce_1$ alloy annealed at 400 °C and 500 °C.

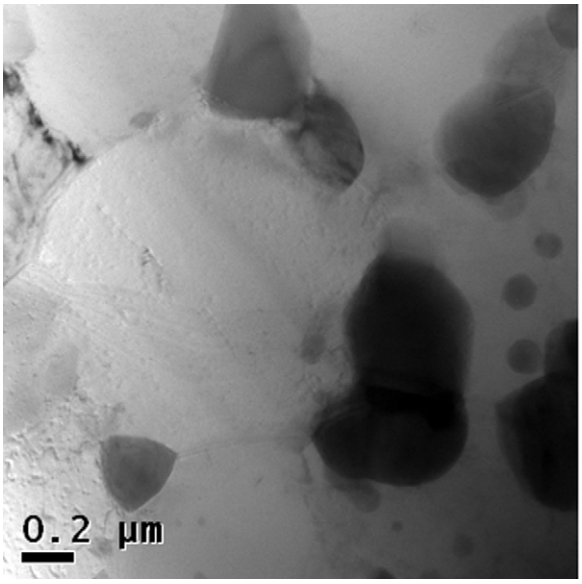

Fig. 6. TEM micrographs of $AlCr_3Fe_3Ce_1$ alloy annealed at 500 °C for 100 h.

Significant structural changes were observed in the alloy annealed at 500 °C. Substantial grain coarsening can be seen in Fig. 6 showing TEM image of the alloy annealed at 500 °C for 100 h. The appearance of Al_3Ce phase was detected in the sample annealed at 500 °C for 100 h by XRD, see Fig. 3c. Moreover, one can see in Fig. 5 that the hardness of the $AlCr_3Fe_3Ce_1$ alloy decreased when annealed at 500 °C down to HV0.02 ≈70, i.e. the value which corresponds to a non-hardened aluminium. Grain size distribution obtained by analysis of TEM images is plotted in Fig. 7. While the grain size distribution in the rapidly solidified alloy and the sample annealed at 400 °C is approximately the same, a significant grain coarsening takes place after annealing at 500 °C. TEM observations are supported by the Rietveld structure refinement of XRD patterns shown in Table 1. Although the absolute grain sizes determined by TEM and XRD differ, the same trend in grain size evolution was observed by TEM and XRD. The grain size remains approximately constant up to 400 °C. Then after annealing at 500 °C grain

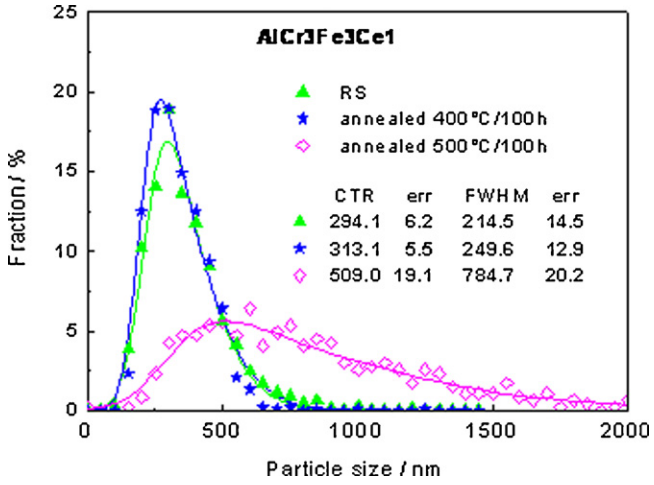

Fig. 7. Grain size distribution determined from TEM micrographs in rapidly solidified $AlCr_3Fe_3Ce_1$ alloy and the alloy annealed at 400 °C and 500 °C for 100 h (CTR – center of the peak, the most common grain size, FWHM – full width at half maximum).

Table 1
The mean grain size determined by Rietveld refinement from XRD patterns for rapidly solidified $AlCr_3Fe_3Ce_1$ alloy and alloy annealed at 400 °C and 500 °C for 100 h.

State of the alloy	Mean grain size (nm)
Rapidly solidified	165 ± 4
Annealed 400 °C/100 h	148 ± 3
Annealed 500 °C/100 h	211 ± 5

growth occurs and grain size becomes approximately two-times higher. Possible explanation of this behavior is that at 400 °C the activation energy for diffusion of alloying elements is not sufficient for any significant change. However at 500 °C the situation changes, diffusivities of Fe, Cr and Ti increase, and recrystallization occurs. It should be mentioned that the Rieltveld structure refinement determines the size of coherently diffracting domains. Thereby, the Rieltveld structure refinement is able to distinguish sub-grains which appear as a single grain in TEM micrographs. For this reason the main grain size estimated by TEM is always higher than the mean domain size determined by XRD.

Results of LT measurements, i.e. lifetimes τ_i and relative intensities I_i of the exponential components resolved in LT spectra, are listed in Table 2. The short-lived component with lifetime τ_1 represents a contribution of free positrons which are not trapped at defects and annihilate from the delocalized state. The component with lifetime τ_2 and dominating intensity comes from positrons trapped at dislocations. Indeed, the lifetime $\tau_2 \approx 245$ ps of this component falls into the range of 220–250 ps reported in literature for positrons trapped in Al dislocations [21–25]. Hence, dislocations are the main structural defects in the rapidly solidified $AlCr_3Fe_3Ce_1$ alloy.

The long-lived component with lifetime τ_3 is caused by orthopositronium (o-Ps), i.e. hydrogen-like bound state of electron and positron [26], which is formed in microvoids. The size of microvoids estimated from the lifetime τ_3 using the Tao–Eldrup model [27,28] is approximately 0.3 nm. Microvoids are formed in the rapidly solidified alloy by clustering of quenched-in vacancies.

Note that Dhanalakshmi et al. [29] observed in Al–Fe–MM (MM = mischmetal) alloys only two LT components with lifetimes ≈216 ps and ≈560 ps, i.e. the component corresponding to positrons trapped at dislocations was not observed. This is probably due to significantly higher cooling rates used in preparation of Al–Fe–MM alloy. The circumferial speed of the cooling wheel in Ref. [29] was more than two times higher than in our case. Also the composition of alloy used in Ref. [29] exhibited higher tendency to form glassy state due to higher total amount of alloying elements in comparison to $AlCr_3Fe_3Ce_1$ alloy. Crystalline matrix is usually not formed under such high cooling rates and high concentration of alloying elements and the rapidly solidified alloy is in amorphous state. Under such conditions dislocation substructure is not formed and positrons are trapped at vacancy-like defects and microvoids existing in the amorphous matrix and with a certain size distribution.

Virtually no change in the sample was detected after annealing at 300 °C for 100 h. The LT spectrum still contains three lifetime components with lifetimes and intensities comparable with those found in the rapidly solidified sample, see Table 2. Annealing at 400 °C leads to disappearance of the long lived o-Ps component, which proves that microvoids are not present in the sample anymore. Most probably the temperature of 400 °C is high enough to break up microvoids. Released vacancies are subsequently recovered by diffusion to sinks.

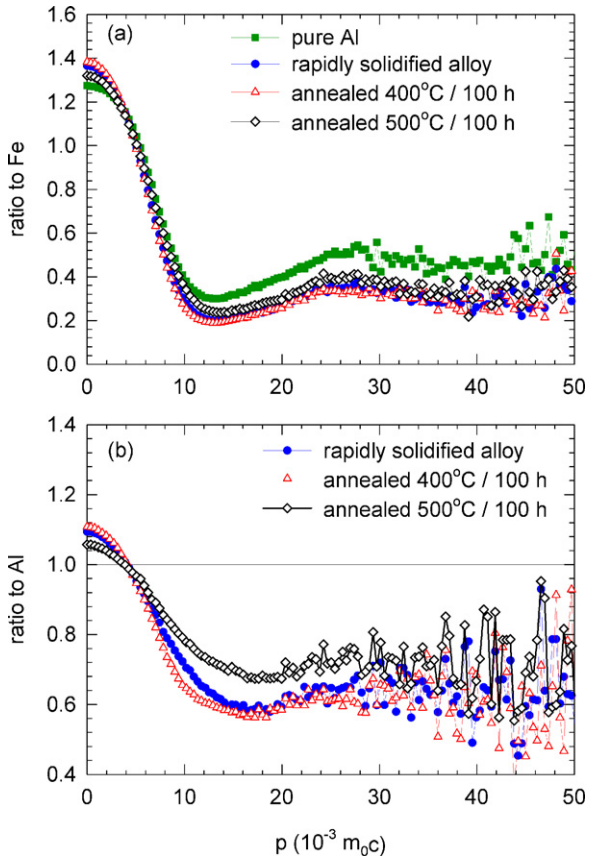

Fig. 8. CBD ratio curves related to (a) well annealed pure Fe, (b) well annealed pure Al, of rapidly solidified $AlCr_3Fe_3Ce_1$ alloy and the alloy annealed at 300 °C, 400 °C and 500 °C for 100 h. The ratio curve (related to pure Fe) for a well annealed pure Al is plotted in the upper panel for comparison.

A decrease in the intensity I_2 of positrons trapped at dislocations occurs only after annealing at 500 °C for 100 h, see Table 2. This gives clear evidence for the onset of recrystallization in the sample accompanied by recovery of dislocations in accordance with the observed decrease in hardness, see Fig. 5. Thus, rapidly solidified $AlCr_3Fe_3Ce_1$ alloy exhibits exceptionally high thermal stability of ultra fine grained structure and dislocations.

The CDB ratio curves (related to pure Fe) for the rapidly solidified $AlCr_3Fe_3Ce_1$ alloy and the alloy annealed at various temperatures are very similar to the curve measured on the reference pure Al specimen, as illustrated in Fig. 8a. It gives clear evidence that positrons annihilate predominantly with Al electrons. This is not surprising taking into account that atomic concentrations of alloying elements – 1.71 at.% Cr, 1.47 at.% Fe, and 0.17 at.% Ce – are rather low. Since majority of positrons annihilate at dislocations, CDB

Table 2
Results of LT spectroscopy: lifetimes τ_i and relative intensities I_i of components resolved in LT spectra measured on rapidly solidified $AlCr_3Fe_3Ce_1$ alloy and the alloy annealed at 300 °C, 400 °C and 500 °C for 100 h. The quantity τ_f calculated from Eq. (1) is shown in the last column.

State of the alloy	τ_1 (ps)	I_1 (%)	τ_2 (ps)	I_2 (%)	τ_3 (ps)	I_3 (%)	τ_f (ps)
Rapidly solidified	116 ± 2	8.7 ± 0.3	243 ± 1	89.6 ± 0.2	880 ± 40	1.7 ± 0.5	225 ± 3
300 °C/100 h	103 ± 3	6.5 ± 0.3	244 ± 1	91.1 ± 0.4	980 ± 50	2.4 ± 0.1	229 ± 4
400 °C/100 h	104 ± 3	7.5 ± 0.1	243 ± 1	92.5 ± 0.2	–	–	221 ± 4
500 °C/100 h	134 ± 5	21 ± 1	258 ± 3	79 ± 1	–	–	216 ± 6

results testify that there is no significant segregation of alloying elements on dislocations. However, compared to the well annealed pure Al reference specimen, the CDB curves of $AlCr_3Fe_3Ce_1$ alloy are enhanced in the low momentum range ($p < 10^{-3}\ m_0c$), whereas in the high momentum range ($p > 10^{-3}\ m_0c$) they are positioned below the Al curve. This difference is better visible in Fig. 8b which shows CDB ratio curves related to well-annealed pure Al. Clearly, the high momentum parts of CDB ratio curves in Fig. 8b are rather flat without any significant features and are positioned well below unity. This is because in the rapidly solidified $AlCr_3Fe_3Ce_1$ alloy the majority of positrons are trapped at dislocations, while in pure Al, almost all positrons annihilate from the free state. Since the overlap of positron wave function with the core electrons is reduced for positrons trapped at defects, the high momentum part of the corresponding CDB curve is depressed. Positrons are annihilated predominantly by Al electrons; therefore the CDB curves do not show any significant features and are simply shifted down in the high momentum range. The CDB curve of the material annealed at 500 °C becomes clearly more similar to the curve of pure Al in agreement with lifetime measurements which revealed a decrease in density of dislocations at this temperature.

4. Estimation of defect density

TEM images clearly showed that spatial distribution of dislocations in rapidly solidified $AlCr_3Fe_3Ce_1$ alloy is not uniform. Dislocation walls with high dislocation density were formed and surround cells exhibiting substantially lower density of dislocations. As will be shown in the next paragraph, non-uniform spatial distribution of dislocation is testified also by LT results.

Kinetics of positron trapping is described using the trapping model, which allows for the determination of defect densities in the sample from LT data. So called simple trapping model (STM) introduced by West [30] describes positron trapping by a simple set of linear differential equations. STM is widely used for modeling of positron trapping and determination of defect densities in various materials. However, it has to be emphasized that STM was developed under several assumptions: (i) only thermalized positrons are trapped at defects, (ii) no detrapping of positrons trapped at defects occurs and (iii) positron trapping rate to each type of defect is constant throughout the whole sample (i.e. positron capture in defect is driven by the quantum mechanics transition from the delocalized to the bound state and the transport of positrons to the vicinity of defect can be neglected – so called transition-limited trapping) [31]. Always it is very important to check whether these assumptions are fulfilled in the particular system before application of STM. Such test of STM applicability can be made using the quantity

$$\tau_f = \left(\sum_i \frac{I_i}{\tau_i} \right)^{-1}, \tag{1}$$

where τ_i and I_i are lifetimes and relative intensities of various positron states resolved in LT spectrum. In the frame of STM the quantity τ_f equals to the bulk lifetime τ_B, i.e. the lifetime of free positrons in a perfect defect-free material. The bulk positron lifetime $\tau_B = 161$ ps was determined in a well annealed Al [22–24]. Note that the quantity τ_f is calculated only from components corresponding to annihilation of positron, i.e. the long lived o-Ps component τ_3 is not included in Eq. (1). The τ_f values obtained from Eq. (1) for the alloys studied are listed in the last column in Table 2. Clearly, in all samples of $AlCr_3Fe_3Ce_1$ alloy τ_f values are significantly higher than τ_B. This testifies that STM assumptions are not fulfilled here. In particular, strongly non-uniform distribution of dislocations in $AlCr_3Fe_3Ce_1$ alloy leads to a spatial dependence of positron trapping rate which violates the assumption (iii). The trapping rate to dislocations for a positron situated inside a dislocation wall is substantially higher than that for positron inside a dislocation-free cell interior. Moreover, positron diffusion from cells into dislocation walls has to be taken into account, i.e. transport of positrons to the vicinity of traps cannot be neglected here.

Proper description of positron trapping in rapidly solidified $AlCr_3Fe_3Ce_1$ alloy can be obtained only using model which takes into account both spatial dependence of trapping rate and the transport of positrons from cells into dislocation walls. Diffusion trapping model (DTM) derived from integration of positron diffusion equation was developed by Dupasquier et al. [32] and successfully applied for description of positron trapping at grain boundaries. The DTM model was further generalized in Ref. [33] to describe positron trapping in ultra fine grained materials prepared by severe plastic deformation. Here we present the DTM model in the form suitable for description of positron trapping in rapidly solidified $AlCr_3Fe_3Ce_1$ alloy.

In the frame of DTM the assumptions (i) and (ii) are still assumed to be fulfilled. However, the assumption (iii) is relaxed and rapidly solidified alloy is represented by spherical domains with radius R separated by dislocation walls with thickness δ. Dislocation walls contain very high density of dislocations ρ_D, while cells are dislocation-free.

There are several channels for positron fate in the sample: firstly it is necessary to separate positrons which formed positronium (Ps) during thermalization and are localized in microvoids. The para-positronium (p-Ps, anti-parallel spins) and ortho-positronium (o-Ps, parallel spins) are formed in the fixed ratio 1:3. Positrons which formed o-Ps annihilate by pick-off annihilation [26,27] and constitute a long-lived component with lifetime $\tau_{\text{o-Ps}}$ in LT spectrum. On the other hand, p-Ps decays by self-annihilation with a short lifetime $\tau_{\text{p-Ps}} = 125$ ps [26]. Hence, time evolution of the number $N_{\text{Ps}}(t)$ of Ps atoms can be written as

$$N_{\text{Ps}}(t) = \xi \left[\frac{1}{4} \exp\left(-\frac{t}{\tau_{\text{p-Ps}}} \right) + \frac{3}{4} \exp\left(-\frac{t}{\tau_{\text{o-Ps}}} \right) \right], \tag{2}$$

where ξ is the fraction of positrons which formed Ps.

Positrons which did not form Ps are stopped either in dislocation walls or inside cells. Because of very high dislocation density in dislocation walls, positrons thermalized there are almost immediately trapped at dislocations and contribute, thereby, to the dislocation component with lifetime τ_D. The probability η that a positron will be stopped inside a dislocation wall equals the volume fraction of dislocation walls

$$\eta = \frac{(R+\delta)^3 - R^3}{(R+\delta)^3}. \tag{3}$$

Positrons which end their thermalization inside cells may either annihilate from the free state inside the cell or may diffuse to dislocation walls surrounding the cell and be trapped in dislocations there. The space and time dependence of the positron density $n(r, t)$ inside the cell is governed by the diffusion equation [32]

$$\frac{\partial n}{\partial t} = D_+ \left(\frac{\partial^2 n}{\partial r^2} + 2\frac{\partial n}{\partial r} \right) - \frac{1}{\tau_B} n, \tag{4}$$

where D_+ is the positron diffusion coefficient. Here we used $D_+ = 1.7 \pm 0.2\ \text{cm}^2\ \text{s}^{-1}$ determined for Al in Ref. [34]. Since positron trapping occurs on the surface of cells, the number of positrons trapped in unit time is

$$T = K_D 4\pi R^2 \delta n(R, t), \tag{5}$$

where K_D is the trapping rate to dislocations for a positron situated inside a dislocation wall. Equivalently T can be expressed also through the density gradient-driving current passing through the

interface between the cell and the dislocation wall

$$T = -4\pi R^2 D_+ \left(\frac{\partial n}{\partial r}\right)_{r=R}. \quad (6)$$

By combining Eqs. (5) and (6) one obtains the boundary condition for the diffusion Eq. (4)

$$\left(\frac{\partial n}{\partial r}\right)_{r=R} = -\frac{\alpha}{R} n(R,t), \quad (7)$$

where the parameter

$$\alpha = \frac{K_D \delta R}{D_+} \quad (8)$$

introduced in Ref. [32] characterizes the balance between the factors limiting positron capture. The limit $\alpha \to \infty$ corresponds to the transition-limited trapping where positron transport to defect can be neglected, while $\alpha = 0$ corresponds to the diffusion-limited capture driven by transport of positron to the vicinity of defect. In rapidly solidified $AlCr_3Fe_3Ce_1$ alloy the parameter α fall in the range 0.4–0.7 indicating that positron trapping in dislocation walls is limited mainly by positron diffusion from cell interior into the walls. The initial condition for diffusion Eq. (4) is

$$n(r,0) = \frac{3(1-\xi)(1-\eta)}{4\pi R^3}. \quad (9)$$

The analytical solution of diffusion Eq. (4) with the boundary and the initial conditions (7) and (9) can be written as

$$n(r,t) = \frac{3(1-\xi)(1-\eta)}{4\pi R^3} \frac{R}{r} \sum_{k=1}^{\infty} a_k \frac{\sin(\beta_k r/R)}{\sin \beta_k} \exp\left(-\frac{t}{\tau_k}\right), \quad (10)$$

where β_k is the kth solution of the eigenvalue equation

$$\beta_k \cot \beta_k + \alpha - 1 = 0, \quad (11)$$

$$a_k = \frac{2\alpha}{\beta_k^2 + \alpha(\alpha-1)}, \quad (12)$$

$$\tau_k = \left(\frac{1}{\tau_B} + \frac{\beta_k^2 D_+}{R^2}\right)^{-1}. \quad (13)$$

The number $N_f(t)$ of free positrons in cells is obtained by spatial integration of the positron density $n(r,t)$

$$N_f(t) = 4\pi \int_0^R n(r,t) r^2 dr, \quad (14)$$

which yields

$$N_f(t) = 3(1-\xi)(1-\eta)\alpha \frac{D_+}{R^2} \sum_{k=1}^{\infty} a_k \frac{\tau_B \tau_k}{\tau_B - \tau_k} \exp\left(-\frac{t}{\tau_k}\right). \quad (15)$$

The rate equation describing the time evolution of the number $N_D(t)$ of positrons trapped in dislocation walls is

$$\frac{dN_D}{dt} = -\frac{1}{\tau_D} N_D + T. \quad (16)$$

The trapping rate

$$T = 3\frac{(1-\xi)(1-\eta)}{R} K_D \delta \sum_{k=1}^{\infty} a_k \exp\left(-\frac{t}{\tau_k}\right)$$

is obtained by inserting the solution (10) into Eq. (5). The initial condition for the rate Eq. (16) is

$$N_D(0) = \eta \quad (17)$$

accounts for the fraction of positrons which ended their thermalization inside dislocation walls. This fraction of positrons equals the volume fraction of dislocation walls defined by Eq. (3). The solution of Eq. (16) can be expressed as

$$N_D = (1-\xi)\eta \exp\left(-\frac{t}{\tau_D}\right) + 3(1-\xi)(1-\eta)\alpha \frac{D_+}{R^2} \times \sum_{k=1}^{\infty} a_k \frac{\tau_D \tau_k}{\tau_D - \tau_k} \left[\exp\left(-\frac{t}{\tau_D}\right) - \exp\left(-\frac{t}{\tau_k}\right)\right]. \quad (18)$$

Hence, the LT spectrum

$$S(t) = -\frac{d}{dt}(N_f + N_D + N_{Ps}) \quad (19)$$

takes the form

$$S(t) = \sum_{k=1}^{\infty} \frac{1}{\tau_k} i_k \exp\left(-\frac{t}{\tau_k}\right) + \frac{1}{\tau_D} I_D \exp\left(-\frac{t}{\tau_D}\right) + \xi\left[\frac{1}{4}\frac{1}{\tau_{p\text{-}Ps}} \exp\left(-\frac{t}{\tau_{p\text{-}Ps}}\right) + \frac{3}{4}\frac{1}{\tau_{o\text{-}Ps}} \exp\left(-\frac{t}{\tau_{o\text{-}Ps}}\right)\right], \quad (20)$$

where

$$i_k = 3\alpha(1-\xi)(1-\eta)\frac{D_+}{R^2} a_k \left(\frac{\tau_B \tau_k}{\tau_B - \tau_k} - \frac{\tau_D \tau_k}{\tau_D - \tau_k}\right), \quad (21)$$

$$I_D = (1-\xi)\eta + 3\alpha(1-\xi)(1-\eta)\frac{D_+}{R^2} \sum_{k=1}^{\infty} a_k \frac{\tau_D \tau_k}{\tau_D - \tau_k}. \quad (22)$$

The LT spectra measured on $AlCr_3Fe_3Ce_1$ alloy were fitted by the model (20) convoluted with the resolution function of spectrometer. Very good agreement of the model function with experimental points was achieved in all samples studied. The fitting parameters here were R, δ, τ_D, K_D, ξ, η, $\tau_{o\text{-}Ps}$, while the quantities $\tau_B = 161$ ps, $\tau_{p\text{-}Ps} = 125$ ps, $D_+ = 1.7\ cm^2\ s^{-1}$ were considered as constants. The infinite sums in the previous equations converge relatively fast. It was found that truncation at $k \geq 10\alpha$ is always acceptable.

The fraction of positrons which formed Ps $\xi = 2.0 \pm 0.5\%$ was found in the rapidly solidified $AlCr_3Fe_3Ce_1$ alloy and the sample annealed at 300 °C. Since the Ps contribution disappeared in the samples annealed at 400 °C and 500 °C, the fraction $\xi = 0$ in these samples.

The thickness of cell walls $\delta = 10 \pm 1$ nm was obtained from fitting of LT spectra of rapidly solidified $AlCr_3Fe_3Ce_1$ alloy. No changes of δ except for statistical scattering could be detected in annealed $AlCr_3Fe_3Ce_1$ alloys. The lifetime τ_D of positrons trapped at dislocations remains also approximately constant during annealing and exhibits only statistical scattering around the mean value $\tau_D = 237 \pm 2$ ps. This testifies that the nature of positron traps, i.e. dislocations, remains unchanged and annealing only changes the concentration of these traps. Interestingly τ_D obtained from fitting of LT spectra in the frame of DTM is slightly lower than the average value of the lifetime $\tau_2 = 247 \pm 4$ ps determined by the simple two-component decomposition, see Table 2. This difference is most probably because DTM more precisely describes the multi-component nature of the short-lived part of LT spectra, while in two-component fitting this part of spectrum is approximated just by a single component with lifetime τ_1. Due to the mutual correlation of the fitting parameters this inaccuracy also slightly influenced the lifetime τ_2. It is well-known [35,36] that dislocation line itself is a shallow positron trap and serves only as a precursor for positron trapping. Pre-trapped positron diffuses quickly along dislocation line (pipe diffusion) and becomes eventually trapped in deep traps, namely jogs on dislocation line or vacancies anchored in compressive elastic field of dislocation [35,36]. Indeed, compared to τ_2, the lifetime τ_D obtained within DTM is closer to the calculated lifetime of positrons trapped in vacancy attached to Al dislocation

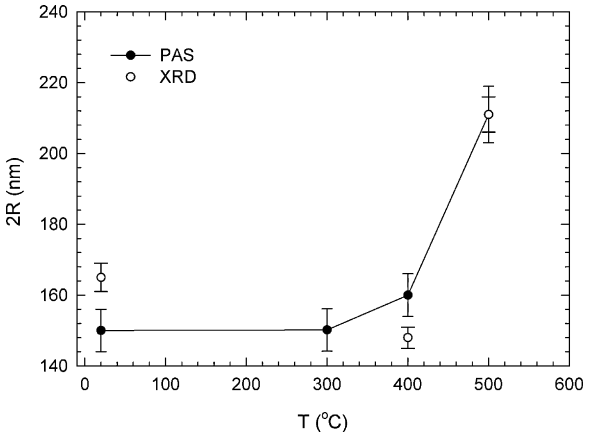

Fig. 9. Temperature dependence of the mean cell size $2R$ obtained from fitting of LT spectra by DTM (full points) and the mean size of coherently diffracting domains determined from the Rietveld analysis of XRD profiles (open points).

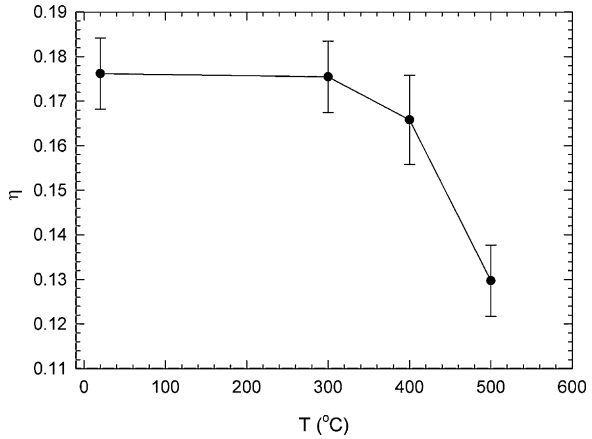

Fig. 10. Temperature dependence of the volume fraction η of dislocation walls obtained from fitting of LT spectra by DTM.

or in a jog on the dislocation line [37]. The dislocation density in walls can be calculated from the positron trapping rate K_D

$$\rho_D = \frac{K_D}{\nu_D}, \tag{23}$$

where ν_D is the specific positron trapping rate (trapping coefficient) for dislocations. Here we use $\nu_D = 0.45 \times 10^{-4}\,m^2\,s^{-1}$ determined for Al dislocations in Ref. [23]. The dislocation density in walls calculated from Eq. (23) is $\rho_D = 2.3 \pm 0.5 \times 10^{15}\,m^{-2}$ and remains practically constant during annealing. This testifies a high dislocation density inside dislocation walls. Virtually no change in ρ_D during annealing indicates that there is no significant recovery or re-arrangement of dislocations inside dislocation walls till the onset of recrystallization at 500 °C.

The cell size $2R$ obtained from fitting of LT spectra is plotted in Fig. 9 as a function of the annealing temperature. The cell size in rapidly solidified $AlCr_3Fe_3Ce_1$ alloy is $2R = 150 \pm 6$ nm. With increasing temperature, $2R$ remains virtually unchanged up to 400 °C, see Fig. 9. This testifies very good thermal stability of ultra fine grained structure of rapidly solidified $AlCr_3Fe_3Ce_1$ alloy. A significant increase of $2R$ was observed in the sample annealed at 500 °C giving a clear evidence that recrystallization takes place in the sample. The size of coherently diffracting domains determined by Rietveld analysis of XRD reflections is plotted in Fig. 9 as well. One can see in the figure that there is a satisfactory agreement between PAS and XRD results.

Temperature dependence of the volume fraction η of dislocation walls is plotted in Fig. 10. The volume fraction η remains approximately constant up to 400 °C. Annealing at higher temperatures causes a significant decrease in the volume fraction of dislocation walls. Obviously this is due to recrystallization in the sample. New virtually defect-free recrystallized grains gradually replace the original ultra fine grained structure with dislocation walls.

5. Conclusions

Microstructure of rapidly solidified $AlCr_3Fe_3Ce_1$ alloy and its thermal stability were investigated in this work by PAS combined with XRD, TEM and hardness measurements. The rapidly solidified $AlCr_3Fe_3Ce_1$ alloy exhibits ultra fine grained structure consisting of fcc-Al, crystalline intermetallic phases, and a small amount of quasicrystalline phase. PAS revealed a high density of dislocations in the rapidly solidified alloy. However, spatial distribution of dislocations is strongly non-uniform: material contains dislocation walls with a high dislocation density forming low-angle grain boundaries and cells containing substantially lower density of dislocations. Besides dislocations, microvoids created by agglomeration of quenched-in vacancies were found in the rapidly solidified alloy.

No structural changes were observed after annealing up to 400 °C. Thus, our results proved that rapidly solidified $AlCr_3Fe_3Ce_1$ alloy exhibits good thermal stability of ultra fine grained structure. The alloy annealed at 500 °C undergoes recrystallization, which is detected by PAS, XRD and also by TEM observations and hardness measurements.

Kinetics of positron trapping in rapidly solidified $AlCr_3Fe_3Ce_1$ alloy was properly described by diffusion trapping model presented in this work. It was demonstrated that the mean cell size determined from LT data using this model agrees well with the average size of coherently diffracting domains obtained from Rietveld refinement of XRD patterns. The cell size obtained by XRD and PAS corresponds to the size of sub-grains which may appear as a single grain in TEM images. Therefore, the mean grain size estimated by TEM is always higher compared to that determined by XRD and PAS. A significant grain growth in the sample annealed at 500 °C was detected by XRD, PAS and also by TEM.

Acknowledgements

This work was financially supported by The Czech Academy of Sciences (project no. KAN 300100801), The Czech Scientific Foundation (project no. P108/10/0648) and The Ministry of Education, Youth and Sports of the Czech Republic (projects nos. MSM6046137302 and MS0021620834).

References

[1] Z. Zhang, Z. Wang, X. Bian, W. Wang, J. Cryst. Growth 281 (2005) 646.
[2] P. Hautojärvi, in: P. Hautojärvi (Ed.), Positrons in Solids, Springer-Verlag, Berlin, 1979.
[3] R.W. Siegel, Ann. Rev. Mater. Sci. 10 (1980) 393.
[4] P. Hautojärvi, C. Corbel, Positron spectroscopy of solids, in: A. Dupasquier, A.P. Mills (Eds.), Proceedings of the International School of Physics "Enrico Fermi" Course CXXV, IOS Press, Amsterdam, 1995, p. 491.
[5] K.G. Lynn, J.R. MacDonald, R.A. Boie, L.C. Feldman, J.D. Gabbe, M.F. Robbins, E. Bonderup, J. Golovchenko, Phys. Rev. Lett. 38 (1977) 241.
[6] A. Somoza, A. Dupasquier, J. Mater. Process. Technol. 135 (2003) 83.
[7] M. Biasini, G. Ferro, P. Folegati, G. Riontino, Phys. Rev. B 63 (2001) 092202.
[8] W. Brandt, Positron solid-state physics, in: W. Brandt, A. Dupasquier (Eds.), Proceedings of the International School of Physics "Enrico Fermi" Course LXXXIII, North Holland, Amsterdam, 1983, p. 1.
[9] M.J. Puska, R.M. Nieminen, Rev. Mod. Phys. 66 (1994) 841.
[10] R.S. Brusa, W. Deng, G.P. Karwasz, A. Zecca, Nucl. Instr. Meth. B 194 (2002) 519.
[11] P. Asoka-Kumar, M. Alatalo, V.J. Ghosh, A.C. Kruseman, B. Nielsen, K.G. Lynn, Phys. Rev. Lett. 77 (1996) 2097.
[12] I. Makkonen, M. Hakala, M.J. Puska, Phys. Rev. B 73 (2006) 035103.

[13] J. Kuriplach, A.L. Morales, C. Dauwe, D. Segers, M. Šob, Phys. Rev. B 58 (1998) 10475.
[14] F. Bečvář, J. Čížek, I. Procházka, J. Janotová, Nucl. Instr. Meth. A 539 (2005) 372.
[15] F. Bečvář, J. Čížek, I. Procházka, Acta Phys. Pol. A 113 (2008) 1279.
[16] F. Bečvář, Nucl. Instr. Meth. B 261 (2007) 871.
[17] I. Procházka, I. Novotný, F. Bečvář, Mater. Sci. Forum 772 (1997) 255.
[18] C. Zhang, Y. Wu, X. Cai, F. Zhao, S. Zheng, G. Zhou, S. Wu, Mater. Sci. Eng. A 323 (2002) 226.
[19] K. Saksl, P. Jóvári, H. Franz, J.Z. Jiang, J. Appl. Phys. 97 (2005) 113507.
[20] M. Yamasaki, Y. Nagaishi, Y. Kawamura, Scr. Mater. 56 (2007) 785.
[21] P. Hautojärvi, A. Tamminen, P. Jauho, Phys. Rev. Lett. 24 (1970) 459.
[22] R.M.J. Cotterill, K. Petersen, G. Trumpy, J. Träff, J. Phys. F: Met. Phys. 2 (1972) 459.
[23] M. Iwami, E. Hashimoto, Y. Ueda, J. Phys.: Condens. Matter 7 (1995) 9935.
[24] J. Čížek, I. Procházka, T. Kmječ, P. Vostrý, Phys. Stat. Sol. (a) 180 (2000) 439.
[25] K. Petersen, I.A. Repin, G. Trumpy, J. Phys. Condens. Matter 8 (1996) 2815.
[26] O.E. Mogensen, Positron Annihilation in Chemistry, Springer-Verlag, Berlin, 1995.
[27] S.J. Tao, J. Chem. Phys. 56 (1972) 5499.
[28] M. Eldrup, D. Lightbody, J.N. Sherwood, Chem. Phys. 63 (1981) 51.
[29] S.R. Dhanalakshmi, T. Nagarjan, S. Ramasamy, S. Srinivasan, J. Phys. Chem. Solids 49 (1988) 15.
[30] R. West, in: P. Hautojärvi (Ed.), Positrons in Solids, Springer-Verlag, Berlin, 1979, p. 89.
[31] W. Brandt, Appl. Phys. 5 (1974) 1.
[32] A. Dupasquier, R. Romero, A. Somoza, Phys. Rev. B 48 (1993) 9235.
[33] J. Čížek, I. Procházka, M. Cieslar, R. Kužel, J. Kuriplach, F. Chmelík, I. Stulíková, F. Bečvář, O. Melikhova, R.K. Islamgaliev, Phys. Rev. B 65 (2002) 094106.
[34] E. Soininen, H. Huomo, P.A. Huttunen, J. Mäkinen, A. Vehanen, P. Hautojärvi, Phys. Rev. B 41 (1990) 6227.
[35] L.C. Smedskjaer, M. Manninen, M.J. Fluss, J. Phys. F: Met. Phys. 10 (1980) 2237.
[36] Y. Kamimura, T. Tsutsumi, E. Kuramoto, Phys. Rev. B 52 (1995) 879.
[37] H. Häkkinen, S. Mäkinen, M. Manninen, Phys. Rev. B 41 (1990) 12441.